

SOLAR CELLS

Conformal quantum dot-SnO₂ layers as electron transporters for efficient perovskite solar cells

Minjin Kim^{1†}, Jaeki Jeong^{2†}, Haizhou Lu^{2†}, Tae Kyung Lee³, Felix T. Eickemeyer², Yuhang Liu², In Woo Choi¹, Seung Ju Choi¹, Yimhyun Jo¹, Hak-Beom Kim¹, Sung-In Mo¹, Young-Ki Kim⁴, Heunjeong Lee⁵, Na Gyeong An⁶, Shinuk Cho⁵, Wolfgang R. Tress⁷, Shaik M. Zakeeruddin², Anders Hagfeldt⁸, Jin Young Kim⁶, Michael Grätzel^{2*}, Dong Suk Kim^{1*}

Improvements to perovskite solar cells (PSCs) have focused on increasing their power conversion efficiency (PCE) and operational stability and maintaining high performance upon scale-up to module sizes. We report that replacing the commonly used mesoporous-titanium dioxide electron transport layer (ETL) with a thin layer of polyacrylic acid-stabilized tin(IV) oxide quantum dots (paa-QD-SnO₂) on the compact-titanium dioxide enhanced light capture and largely suppressed nonradiative recombination at the ETL-perovskite interface. The use of paa-QD-SnO₂ as electron-selective contact enabled PSCs (0.08 square centimeters) with a PCE of 25.7% (certified 25.4%) and high operational stability and facilitated the scale-up of the PSCs to larger areas. PCEs of 23.3, 21.7, and 20.6% were achieved for PSCs with active areas of 1, 20, and 64 square centimeters, respectively.

Efforts to realize metal halide perovskite solar cells (PSCs) with power conversion efficiencies (PCEs) of >23% have focused on formamidinium-rich lead iodide (FAPbI₃) formulations (1–7) because their narrower bandgap is closer to the Shockley-Queisser optimum than for methylammonium-based or mixed-halide perovskites (8). By fully using the broad absorption spectrum of FAPbI₃, a certified PCE of 25.21% with a short-circuit current density (J_{sc}) of >26 mA/cm² was obtained for the mesoporous-structure PSCs (7). However, the mesoporous-TiO₂ (m-TiO₂) electron transport layer (ETL) may show unwanted photocatalytic effects under ultraviolet (UV) light illumination, and the low electron mobility of m-TiO₂ limits the charge transport (9–11).

Among alternative metal oxide ETLs (10–17) for PSCs, SnO₂-based PSCs could potentially be more efficient and stable given that SnO₂ is UV resistant and has a higher carrier mobility

than TiO₂, which facilitates electron extraction and transport (10–12). Several techniques, such as spin coating (11, 16), atomic layer deposition (1), and chemical bath deposition (CBD) (12, 17), have been used to deposit the SnO₂ ETLs. Spin-coated SnO₂ ETL from a SnO₂ colloidal quantum dot (QD-SnO₂) solution onto the indium-doped tin oxide (ITO) substrate enabled a certified PCE of >23% for the corresponding planar-structure PSCs (2, 16). Recently, a thin SnO₂ ETL on fluorine-doped tin oxide (FTO) deposited with a well-controlled CBD method enabled PSCs with a certified PCE of 25.19%, because of the improved carrier properties of SnO₂ ETL (17). However, compared with the m-TiO₂-based PSCs, the SnO₂-based PSCs still suffered from a relatively low J_{sc} of <26 mA/cm², which is attributed to the optical losses arising from reflection and destructive interference of the incident light waves at the interfaces.

One approach to reduce these optical losses is to use the textured surface of FTO as the front contact that scatters the incoming radiation, destroying the coherence of the incoming light and affording light trapping by increasing the optical path length (18). The enhanced light absorption by the perovskite benefits the photocurrent delivered by the photovoltaic (PV) cell. Similar strategies have been used for textured crystalline silicon-based PSCs (19). However, early efforts to deposit a thin, uniform, and high-quality SnO₂ ETL using a solution process were incompatible with the underlying textured FTO surface (1, 12, 20–22), causing optical losses. The highest reported J_{sc} of SnO₂-based PSCs of ~25.2 mA/cm² (17, 20) still limits the overall PV performance.

Here we introduce an architecture for the ETL of PSCs that consists of a compact-TiO₂ (c-TiO₂) blocking layer covered by a thin layer of polyacrylic acid (PAA)-stabilized QD-SnO₂ (paa-QD-SnO₂) deposited in a contiguous and

conformal manner on the textured FTO. The uniform bilayer of paa-QD-SnO₂@c-TiO₂ largely improved the perovskite's absorption of sunlight and formed an outstanding electron-selective contact with the perovskite film. The quantum size effect increased the bandgap of the QD-SnO₂ from 3.6 eV for bulk SnO₂ to ~4 eV (21, 23) and produced a corresponding upward shift of its conduction band edge energy. This shift aligned it well with the conduction band edge of the perovskite so that electron capture by the SnO₂-based ETL proceeded with minimal energy losses (5, 11, 16, 21).

PAA, a polymer binder, was added to the SnO₂ QD solution to attach the colloidal QD-SnO₂ firmly to the c-TiO₂ surface, providing a contiguous, thin, and conformal SnO₂ layer that fully covered the c-TiO₂ layer underneath. The carboxyl groups of PAA undergo strong hydrogen and coordinative bonding with the metal oxide surface, facilitating the lamination process, especially for production on a large scale (24–26). By choosing FTO substrates with suitable diffuse transmittance and reflectance, the textured paa-QD-SnO₂@c-TiO₂ bilayer enabled a PCE of 25.7% (certified 25.4%) with a J_{sc} of 26.4 mA/cm² and high stability for the corresponding PSCs. We further demonstrate that the paa-QD-SnO₂@c-TiO₂ bilayer could be applied to realize large PSC modules with an active area up to 64 cm² while maintaining a PCE of >20%.

We investigated the microstructures of the spin-coated QD-SnO₂ layer on the c-TiO₂ using commercially available SnO₂ colloidal QDs with and without PAA. Unless otherwise noted, the QD-SnO₂ solution was diluted by deionized water (1:20) in this study. Figure S1, A to C, shows the top-view scanning electron microscope (SEM) images of the c-TiO₂, QD-SnO₂@c-TiO₂, and paa-QD-SnO₂@c-TiO₂, respectively. Because of the textured surface, the c-TiO₂ layer was not fully covered by the spin-coated QD-SnO₂ (fig. S1B). In contrast, a uniform, conformal paa-QD-SnO₂ layer was formed (fig. S1C). Atomic force microscopy images (fig. S1, D to F) further confirmed the uniform morphology of the paa-QD-SnO₂@c-TiO₂ (fig. S1F), which is different from that of the QD-SnO₂@c-TiO₂ (fig. S1E).

Figure 1, A and B, shows the cross-sectional transmission electron microscopy (TEM) images of the QD-SnO₂@c-TiO₂ and paa-QD-SnO₂@c-TiO₂ bilayers on FTO substrates, respectively. The QD-SnO₂@c-TiO₂ bilayer presented an ununiform distribution over the FTO surface with a thickness that varied from ~30 (vertex region) to ~70 nm (valley region), while the paa-QD-SnO₂@c-TiO₂ bilayer had a uniform and conformal distribution over the FTO surface with a uniform thickness of ~30 nm. The different distribution between QD-SnO₂ and paa-QD-SnO₂ layers can also be seen clearly from the cross-sectional SEM images (fig. S2, A and B),

¹Ulsan Advanced Energy Technology R&D Center, Korea Institute of Energy Research, Ulsan 44776, Republic of Korea. ²Laboratory of Photonics and Interfaces, Institute of Chemical Sciences and Engineering, École Polytechnique Fédérale de Lausanne (EPFL), CH-1015 Lausanne, Switzerland. ³Photovoltaics Research Department, Korea Institute of Energy Research (KIER), Daejeon 34129, Republic of Korea. ⁴Central Research Facilities (UCRF), Ulsan National Institute of Science and Technology (UNIST), Ulsan 44919, Republic of Korea. ⁵Department of Physics and Energy Harvest Storage Research Center, University of Ulsan, Ulsan 44610, Republic of Korea. ⁶Department of Energy Engineering, School of Energy and Chemical Engineering, Ulsan National Institute of Science and Technology (UNIST), Ulsan 44919, Republic of Korea. ⁷Novel Semiconductor Devices Group, Institute of Computational Physics, Zurich University of Applied Sciences, 8401 Winterthur, Switzerland. ⁸Department of Chemistry, Ångström Laboratory, Uppsala University, 751 20 Uppsala, Sweden.

*Corresponding author. Email: michael.gratzel@epfl.ch (M.G.); kimds@kier.re.kr (D.S.K.)

†These authors contributed equally to this work.

suggesting that PAA played a key role in forming the uniform and contiguous layer of paa-QD-SnO₂ ETL, as shown in fig. S3.

Element mapping with energy-disperse x-ray spectroscopy of Ti (Fig. 1, C and D) and Sn (Fig. 1, E and F) revealed a coverage of TiO₂ and SnO₂ over the FTO surface for both QD-SnO₂@c-TiO₂ and paa-QD-SnO₂@c-TiO₂ bilayers. The selected-area electron diffraction generated by TEM for the paa-QD-SnO₂@c-

TiO₂ bilayer (fig. S4) showed that both QD-SnO₂ and c-TiO₂ were polycrystalline. The paa-QD-SnO₂ had a particle size of ~4 nm (fig. S4C), which is also confirmed by the TEM images (fig. S5, A to C) and dynamic light scattering analysis (fig. S5, D and E).

The interactions between PAA and QD-SnO₂ were studied by the x-ray photoelectron spectroscopy (XPS) (fig. S6) and Fourier transform infrared spectroscopy (FTIR) measurements

(fig. S7). It is clear from the XPS measurements that both QD-SnO₂@c-TiO₂ and paa-QD-SnO₂@c-TiO₂ bilayers showed characteristic peaks attributed to Sn (fig. S6A); however, the Sn 3d peaks of paa-QD-SnO₂ shifted to high binding energy by ~0.2 eV compared with that of QD-SnO₂, indicating that PAA was bonded to the QD-SnO₂. No obvious difference was observed for the O 1s characteristic peaks (fig. S6, B to D). FTIR measurements showed

Fig. 1. Microstructures of the ETLs.

(A and B) The cross-sectional TEM images of QD-SnO₂@c-TiO₂ (A) and paa-QD-SnO₂@c-TiO₂ (B) over the FTO substrates. Scale bars, 0.1 μ m. (C and D) EDS elemental analysis of Ti for both QD-SnO₂@c-TiO₂ (C) and paa-QD-SnO₂@c-TiO₂ (D) over the FTO surface. Scale bars, 100 nm. (E and F) EDS elemental analysis of Sn for both QD-SnO₂@c-TiO₂ (E) and paa-QD-SnO₂@c-TiO₂ (F) over the FTO surface. Scale bars, 100 nm.

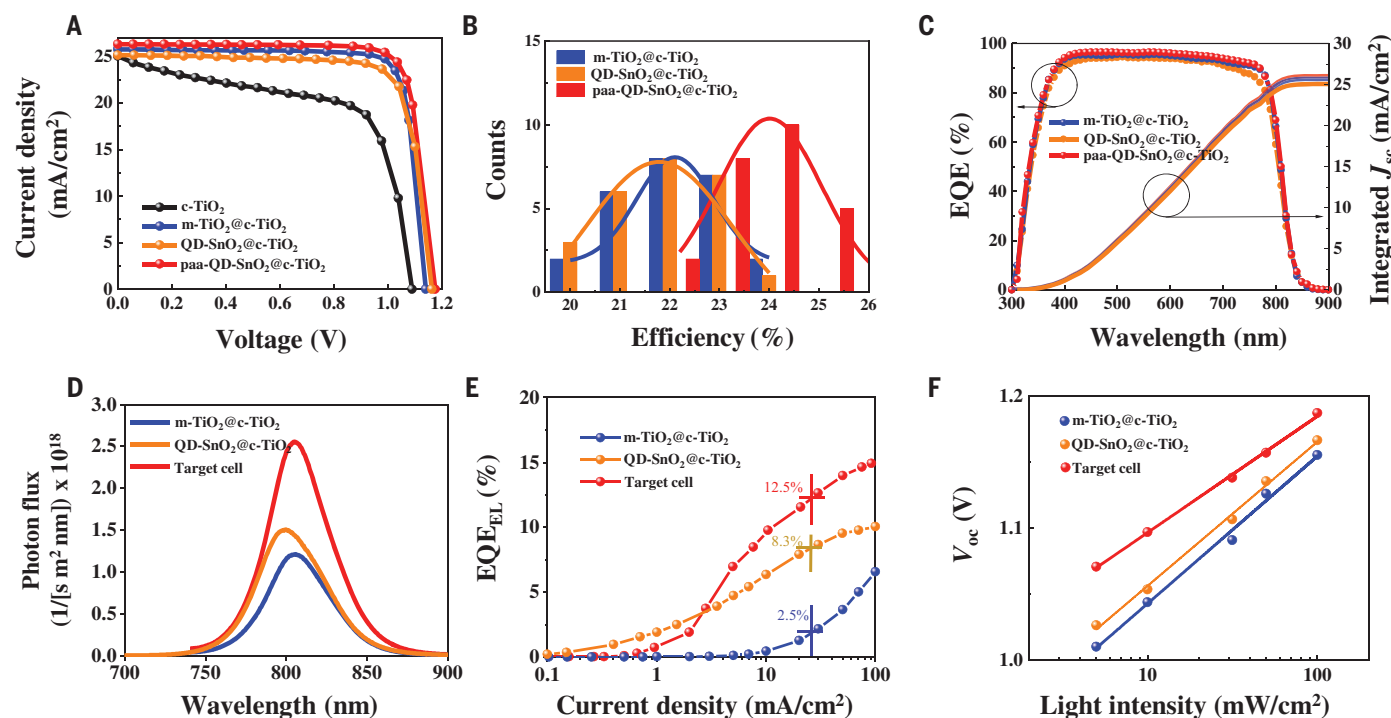
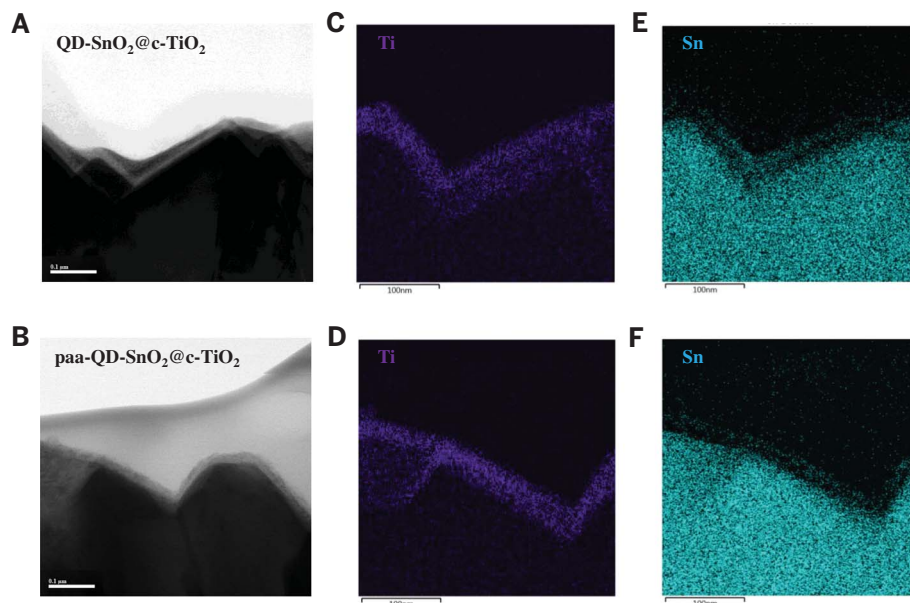


Fig. 2. Characterization of the PSCs. (A) The J-V curves of the PSCs with different ETLs measured under the QSS-IV method. (B) A statistical distribution of the PCE for PSCs with different ETLs. (C to F) The EQE and integrated J_{sc} (C), steady-state PL spectral photon flux (D), EQE_{EL} (E), and the light-dependent V_{oc} (F) for the PSCs with different ETLs.

peaks at ~ 2954 and ~ 1716 cm^{-1} that arise from C–H and C=O stretching vibrations of PAA (fig. S7A) and a characteristic peak at ~ 574 cm^{-1} of the Sn–O vibration (fig. S7B). The Sn–O peak shifted to ~ 594 cm^{-1} for the paa-QD-SnO₂, and the C–H and C=O stretching vibrations shifted to ~ 3012 and ~ 1628 cm^{-1} , respectively (fig. S7C), demonstrating that PAA interacted with QD-SnO₂ (27).

We chose FAPbI₃ as the perovskite layer, and details of its fabrication can be found in the supplementary materials (SM) or a previous report (3). Top-view SEM images of the FAPbI₃ films spin-coated on different ETLs, including c-TiO₂, m-TiO₂@c-TiO₂, QD-SnO₂@c-TiO₂, and paa-QD-SnO₂@c-TiO₂, are shown in fig. S8, A to D, respectively. Compact and dense surface morphologies were observed for all the perovskite films. Figure S9A showed identical x-ray diffraction (XRD) peak positions for all samples at 14.1° and 28.2° , which correspond to the (001) and (002) crystal planes of α -FAPbI₃ (3–5). All the perovskite films had identical full width at half maximum for the main (001) peak (fig. S9B). We conclude that the morphology and crystallinity of the perovskite films are not affected substantially by the different ETLs.

The PSCs with an active area of 0.08 cm^2 were fabricated in a conventional n-i-p structure, FTO/ETL/perovskite/OAI/spiro-MeOTAD/Au, where OAI is octylammonium iodide and spiro-MeOTAD is 2,2',7,7'-tetrakis[N,N-di(4-methoxyphenyl)amino]-9,9'-spirobifluorene. We performed the quasi-steady-state current-voltage (QSS-*I*/*V*) measurement (Fig. 2A), which was used for the certification of PSCs by the National Renewable Energy Laboratory (NREL) and Newport Inc. Details of the QSS-*I*/*V* measurements are given in the SM. All the PSCs were fully aged in the ambient condition for 100 hours before the measurements.

The c-TiO₂-based cell had a low PCE of 17.27% under the QSS-*I*/*V* measurement. For the m-TiO₂@c-TiO₂-based PSC, a PCE of 23.74% with a J_{sc} of 25.74 mA/cm^2 , an open-circuit voltage (V_{oc}) of 1.142 V, and a fill factor (FF) of 80.79% was obtained, which are consistent with the previous reports (3, 7). Compared with the mesoporous-structured devices, the QD-SnO₂@c-TiO₂-based cell had a higher V_{oc} of 1.164 V but a lower J_{sc} of 25.12 mA/cm^2 , resulting in a PCE of 23.29%. The J_{sc} of the QD-SnO₂@c-TiO₂-based PSC is similar to the values reported for the SnO₂-based cells in the literature (17, 20). With the paa-QD-SnO₂@c-TiO₂ ETL, the PSC exhibited a high PCE of 25.18% with a considerably improved J_{sc} of 26.28 mA/cm^2 , V_{oc} of 1.177 V, and FF of 81.49%, matching the 25.39% efficiency certified by Newport Inc. (figs. S10 and S11).

The conventional *J*-*V* measurements under both forward and reverse scans were also performed (fig. S12). The detailed PV parameters

are summarized in table S1. A substantially different PV value was obtained for the c-TiO₂-based cell under QSS-*I*/*V* (Fig. 2A) and conventional *J*-*V* measurements (fig. S12A), whereas the other cells showed similar PV results, indicating that the c-TiO₂-based cell is unstable and that the single c-TiO₂ layer is not a proper ETL for PSCs (28, 29). The contrasting feature of the c-TiO₂-based cell compared with the other cells in Fig. 2A and fig. S12A is discussed in note 1 of the SM. Hereafter, the c-TiO₂-based cells will not be discussed. A statistical distribution of the PCE of all the PSCs (Fig. 2B) shows that the paa-QD-SnO₂@c-TiO₂-based PSC had the highest averaged values. Details of the statistical PV parameters of all different ETL-based cells are shown in fig. S13. The paa-QD-SnO₂@c-TiO₂-based cell is the target of the discussions that follow.

The J_{sc} of the PSCs measured under the solar simulator was verified with external quantum efficiency (EQE) measurements. The target cell had slightly higher EQE than the m-TiO₂@c-TiO₂-based PSC over the entire absorption spectrum (Fig. 2C), resulting in a higher integrated J_{sc} of 26.01 mA/cm^2 ; however, a relatively lower integrated J_{sc} of 25.06 mA/cm^2 was obtained for the QD-SnO₂@c-TiO₂-based device than for the m-TiO₂@c-TiO₂-based cell (25.69 mA/cm^2). The high J_{sc} of the target cell was attributed to the desired light scattering that prolongs the optical length, enhancing the light absorption by the perovskite with the conformal structured paa-QD-SnO₂@c-TiO₂ bilayer over the FTO substrate. This is confirmed with the highest diffuse transmittance (haze) of paa-QD-SnO₂@c-TiO₂ when compared with the other ETLs shown in fig. S14A. The higher transmittance of paa-QD-SnO₂@c-TiO₂ than the QD-SnO₂@c-TiO₂ (fig. S14B) may be traced back to the thinner film thickness, as shown in the optical simulations (fig. S14, C and D), which could also contribute to the high J_{sc} . We further compared the J_{sc} obtained for the paa-QD-SnO₂@c-TiO₂-based PSCs using different substrates (fig. S15). The Asahi FTO glass with high diffuse transmittance was the most suitable substrate for achieving a high J_{sc} .

The effect of the ETL composition on the photon flux emitted by the PSCs measured in steady state at an excitation photon flux equivalent to 1 sun is shown in Fig. 2D. The investigated devices were complete solar cells without the Au back contact. Compared with the m-TiO₂@c-TiO₂- and QD-SnO₂@c-TiO₂-based devices, the target cell had much higher photoluminescence (PL) intensity, reaching a PL quantum yield (PLQY) of 7.5%. This indicates a reduced nonradiative recombination at the interface between perovskite and paa-QD-SnO₂ ETL. Details of the measurements and calculations of PLQY are shown in SM note 2. From the PLQY measurements, we derived

the quasi-Fermi level splitting (ΔE_{F}) in the perovskite under 1 sun illumination (SM note 3) and compared the (ΔE_{F}) with the V_{oc} measured from the same device. ΔE_{F} and V_{oc} showed the same trend, indicating that the V_{oc} increase can be partly attributed to the reduced nonradiative recombination. The $\Delta E_{\text{F}}/q - V_{\text{oc}}$ offset (where q is the elementary charge), however, is different. For the target cell, it is 10 mV lower than that of the m-TiO₂@c-TiO₂-based cells, indicating a better energetic alignment at the interfaces (30).

Ultraviolet photoelectron spectroscopy (UPS) measurements on the surface of different ETLs (fig. S16) showed that the conduction band of paa-QD-SnO₂ matched better with perovskite than the m-TiO₂@c-TiO₂, which could facilitate the charge transfer from perovskite to the ETL (fig. S17). Detailed analysis of the UPS data is shown in SM note 4. Figure S18, A and B, shows the time-resolved PL (TRPL) spectra of the perovskite films on different ETLs measured from both the perovskite and the glass sides. The perovskite film deposited on paa-QD-SnO₂@c-TiO₂ had the fastest decay among all the samples. Because it has a low non-radiative recombination rate, the fast decay is dominated by the favored interfacial electron transfer. The electron mobility measurements (fig. S18C) revealed that the paa-QD-SnO₂@c-TiO₂ layer had the highest carrier mobility. All these results indicate a superior charge extraction from perovskite to the paa-QD-SnO₂ ETL.

Regarding the reduced nonradiative recombination, we determined the EQE of electroluminescence (EQE_{EL}) on representative PSC devices. Figure 2E shows an EQE_{EL} of 12.5% for the target cell at an injection current density of 26 mA/cm^2 corresponding to the J_{sc} under 1 sun illumination, whereas the m-TiO₂@c-TiO₂- and QD-SnO₂@c-TiO₂-based cells have an EQE_{EL} of 2.5 and 8.3%, respectively, under the same conditions. Thus, the nonradiative recombination rate in the PSC was reduced by 80% simply by replacing the m-TiO₂ with a paa-QD-SnO₂ electron-selective contact layer. The highest obtained V_{oc} of 1.22 V (fig. S19), which is near the V_{oc} predicted from EQE_{EL} according to the reciprocity theorem (31, 32), measured without the metal mask reached 98% of the radiative limit V_{oc} (1.25 V) (2, 5). We also conducted transient photovoltage measurements for the PSCs (fig. S20A). The target cell showed a slower V_{oc} decay than the reference cells, indicating a slower charge recombination rate. The dark *J*-*V* curves (fig. S20B) showed the lowest reverse saturation current for the target cell, pushing the onset of the dark current to the highest voltages, which also reflected the lowest interfacial nonradiative recombination.

Figure 2F shows the light intensity-dependent V_{oc} measurements for the PSCs. For both the reference and target cells, the

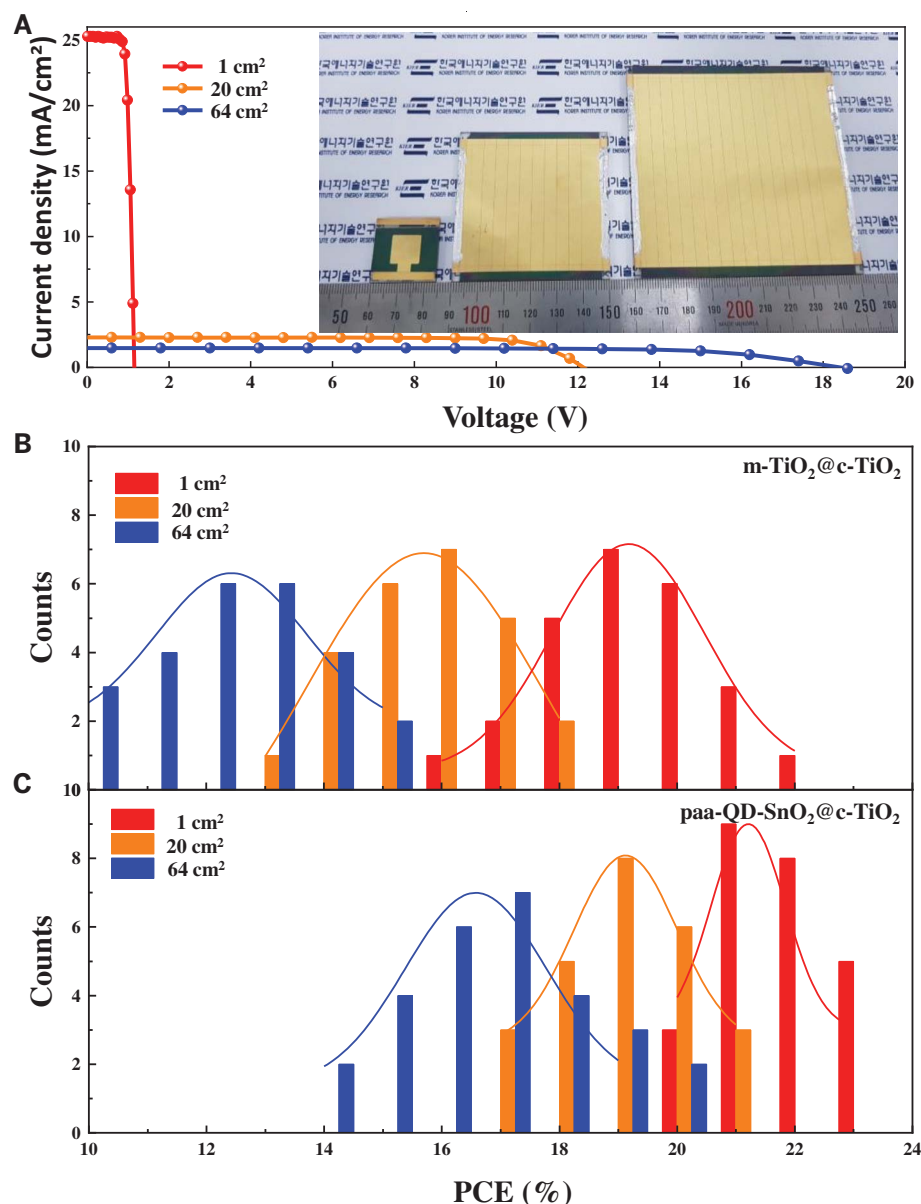


Fig. 3. Performance of the large-size PSCs. (A) *J-V* curves of the large-size PSCs. (Inset) Photo of the large-size PSCs. (B and C) Statistical distributions of the PCEs for the m-TiO₂@c-TiO₂-based (B) and paa-QD-SnO₂@c-TiO₂-based (C) PSCs with pixel sizes of 1, 20, and 64 cm².

measured V_{oc} was linearly dependent on the logarithm of the light intensity. The diode ideality factor n_{id} , deduced from the slope described by $n_{id}k_B T/q$, where k_B is the Boltzmann constant and T is temperature, was 1.83, 1.79, and 1.46 for the m-TiO₂@c-TiO₂- and QD-SnO₂@c-TiO₂-based cells and the target cell, respectively. The reduced n_{id} contributed to the increased FF of the target cell, as the FF critically depends on the n_{id} (33). The reduced n_{id} is also consistent with the PLQY, TRPL, EQE_{EL}, transient photovoltage decay, and dark *J-V* measurements, unambiguously supporting the conclusion of reduced nonradiative recombination of the target PSC using paa-QD-SnO₂

ETL. The decreased nonradiative recombination manifests itself by much stronger photo- and electroluminescence (Fig. 2, C and D) as well as a lower ideality factor (Fig. 2E) enabling very high fill factor of 83.8% to be reached by our target device (table S2). Further strong support for our conclusion comes from the observation of a slower transient photovoltage decay (fig. S20A) and higher electron mobility (fig. S20B) as well as the dark *J-V* measurements of the paa-QD-SnO₂@c-TiO₂-based cell compared with the control devices. The substantial reduction of the trap-assisted nonradiative recombination is the main reason for the reduced V_{oc} deficit of our target

cell of ~310 mV as compared with ~350 mV for the mesoporous-structure cell [bandgap of our perovskite film was calculated to be 1.53 eV (3)], which is one of the lowest values reported in the field of PSCs.

Scale-up of the PSCs to module size is another requirement for their commercial exploitation. We used paa-QD-SnO₂@TiO₂ ETL to fabricate perovskite solar mini-modules with active areas up to 64 cm². Details of the fabrication process for the solar modules can be found in the SM and movie S1. Figure 3A shows the *J-V* curves and images of the perovskite mini-modules with different active areas. The highest PCEs achieved for the PSCs with active areas of 1, 20, and 64 cm² were 23.3, 21.7, and 20.6%, respectively. Movie S2 shows a typical measurement for the 64 cm² perovskite solar modules. Figure S21A illustrates a solar module with subcells connected in series with a magnified view of the contact connections, and a geometrical FF (GFF) was calculated to be 95.6% according to the SEM images (fig. S21B) of the interconnections. Details of the PV parameters are summarized in table S2. The decrease of the PCE with increased device size is mainly caused by a decreased FF. The V_{oc} of the module (table S2) divided by the number of stripes is 18.5 V/16 = 1.156 V, which is equal to the V_{oc} of the 1 cm² cell. Hence, there is no additional V_{oc} loss in the module. Therefore, we attribute the FF decrease to the increased series resistance, including transport layer resistances, contact resistances, and interconnect resistance. We sent the PSC modules to an independent laboratory (OMA Company, Republic of Korea) for certification. PCEs of 21.66% (fig. S22) and 20.55% (fig. S23) were confirmed for the PSC mini-modules with active areas of 20 and 64 cm², respectively, which agreed well with the measurements in our laboratory, and are compared with other reported values in fig. S24.

We further compared the statistical distribution of the PCEs for the mesoporous-based (Fig. 3B) and target (Fig. 3C) perovskite mini-modules. For the perovskite modules with the same active area (1, 20, or 64 cm²), the target modules had higher averaged PCE and narrower PCE distributions than the mesoporous-based modules. The averaged PCE of the 64 cm² PSC module increased by ~30% by simply replacing the m-TiO₂ with paa-QD-SnO₂, indicating that the paa-QD-SnO₂ could be uniformly coated on the large-size substrates. The statistical distribution of the PV parameters (fig. S25) further revealed that the V_{oc} and FF of the mesoporous-based modules decreased significantly more than that of the target PSC modules. The shunt resistance of our solar modules retained a typical value of >4000 ohms-cm² (table S3), indicating that losses from leakage currents across shunts

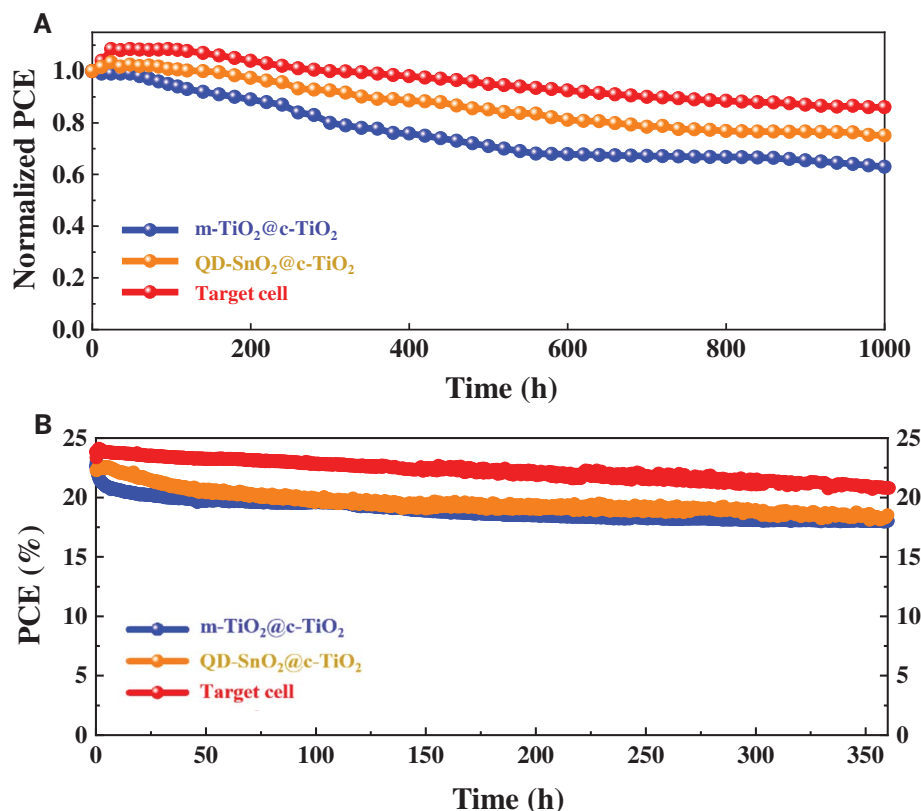


Fig. 4. Stability of the PSCs with different ETLs. The stability shown here represents the best stability results of our four tested samples. **(A)** Shelf life of the unencapsulated PSCs tested in ambient air at 25% RH and 25°C with different ETLs. **(B)** The operational stability test of the unencapsulated PSCs under MPP tracking conditions in a N₂ environment.

produced during scale-up are negligible. We attribute the small decrease of V_{oc} and FF for the target PSC modules to the low contact resistance (fig. S26, A and B) because of the easier laser scribing as well as low series resistance and low interfacial defects of the paa-QD-SnO₂@c-TiO₂ bilayer.

Figure 4A shows the 1000-hour shelf life tested with unsealed devices in ambient air at 25% relative humidity (RH) and 25°C. The target PSC retained 80% of the maximum PCE (25.7%) after 1000-hour storage, whereas the m-TiO₂@c-TiO₂- and QD-SnO₂@c-TiO₂-based PSCs decreased to almost 30 and 40% of the initial efficiency, respectively, indicating that the target cell is more resistant to the moisture and oxygen than the widely used mesoporous structured PSCs. We also performed the operational stability test for the unsealed devices in a N₂ environment under maximum power point (MPP) tracking conditions using a light-emitting diode lamp with a calibrated light intensity of 100 mW/cm². More details about the MPP tests can be found in the SM and in previous reports (5, 7). Figure 4B shows that the target cell had higher PCE than the reference cell during the 350-hour MPP tracking test. From the detailed PV parameters during the MPP tracking measure-

ments (fig. S27), it is clear that the higher performance of the target PSC is due to the higher and rather stable V_{oc} , which decreased less compared with the reference cells. The main degradation of the target cell is the decline of FF (fig. S27), which is attributed to the de-doping of lithium from the hole-transport layer (HTL) (5, 34).

We further tested the sealed devices under ambient conditions. Figure S28 shows that 70.5% of the initial efficiency of the target cell was retained after 700-hour light-soaking test, whereas the efficiency of the m-TiO₂@c-TiO₂-based cell declined 45% over the same testing time. To assess the suitability of the cells for real applications, we performed an MPP stability test for the encapsulated target cell under ambient conditions. Figure S29 shows that 95% of the initial efficiency was retained for the sealed target cell after 100 hours MPP tracking and 2 hours dark recovery under ambient conditions. The substantial decline of FF is still the main reason for the performance loss. Future studies of additive-free HTLs will be conducted to enhance the stability of PSCs.

REFERENCES AND NOTES

1. S. H. Turren-Cruz, A. Hagfeldt, M. Saliba, *Science* **362**, 449–453 (2018).
2. Q. Jiang et al., *Nat. Photonics* **13**, 460–466 (2019).

3. M. Kim et al., *Joule* **3**, 2179–2192 (2019).
4. H. Min et al., *Science* **366**, 749–753 (2019).
5. H. Lu et al., *Science* **370**, eabb8985 (2020).
6. H. Lu, A. Krishna, S. M. Zakeeruddin, M. Grätzel, A. Hagfeldt, *iScience* **23**, 101359 (2020).
7. J. Jeong et al., *Nature* **592**, 381–385 (2021).
8. G. E. Eperon et al., *Energy Environ. Sci.* **7**, 982–988 (2014).
9. T. Leijtens et al., *Nat. Commun.* **4**, 2885 (2013).
10. Q. Jiang, X. Zhang, J. You, *Small* **14**, e1801154 (2018).
11. Q. Jiang et al., *Nat. Energy* **2**, 16177 (2017).
12. E. H. Anaraki et al., *Energy Environ. Sci.* **9**, 3128–3134 (2016).
13. R. Chen et al., *J. Am. Chem. Soc.* **141**, 541–547 (2019).
14. S. S. Shin et al., *Nat. Commun.* **6**, 7410 (2015).
15. S. S. Shin et al., *Science* **356**, 167–171 (2017).
16. G. Yang et al., *Nat. Photonics* **15**, 681–689 (2021).
17. J. J. Yoo et al., *Nature* **590**, 587–593 (2021).
18. S. Manzoor, Z. J. Yu, A. Ali, W. Ali, Z. C. Holman, "Improved light incoupling in planar solar cells via improved texture morphology of PDMS scattering layer," 2017 IEEE 44th Photovoltaic Specialist Conference (PVSC) (2017), pp. 1228–1232.
19. Y. Hou et al., *Science* **367**, 1135–1140 (2020).
20. Y. Zhang et al., *ACS Energy Lett.* **5**, 360–366 (2020).
21. M. M. Tavakoli, F. Giordano, S. M. Zakeeruddin, M. Grätzel, *Nano Lett.* **18**, 2428–2434 (2018).
22. T. Bu et al., *Nat. Commun.* **9**, 4609 (2018).
23. A. Das et al., *J. Mater. Chem. C* **2**, 164–171 (2014).
24. B. Hu et al., *J. Power Sources* **416**, 125–131 (2019).
25. L. Wei, Z. Hou, *J. Mater. Chem. A* **5**, 22156–22162 (2017).
26. P. Parikh et al., *Chem. Mater.* **31**, 2535–2544 (2019).
27. D. Yang et al., *Nat. Commun.* **9**, 3239 (2018).
28. J. Ji et al., *iScience* **23**, 101013 (2020).
29. M. M. Tavakoli, P. Yadav, R. Tavakoli, J. Kong, *Adv. Energy Mater.* **8**, 1800794 (2018).
30. P. Caprioglio et al., *Adv. Energy Mater.* **9**, 1901631 (2019).
31. U. Rau, *Phys. Rev. B* **76**, 085303 (2007).
32. W. Tress et al., *Adv. Energy Mater.* **5**, 1400812 (2015).
33. M. A. Green, *Solar Cells* **7**, 337–340 (1982).
34. Y. Wang et al., *Science* **365**, 687–691 (2019).

ACKNOWLEDGMENTS

We thank B. I. Carlsen, O. Ouellette, and M. Wei for discussions. We thank S. Song for the help of optical simulations. **Funding:** This work was supported by Development Program of the Korea Institute of Energy Research (KIER) (C1-2401 and C1-2402); Basic Science Research Program through the National Research Foundation of Korea (NRF) funded by the Ministry of Education (NRF-2020R1A6A1A03038697); and the NRF funded by the Ministry of Science, ICT, and Future Planning (2020M1A2A2080746 and 2020M1A2A208075011). M.G. acknowledges financial support from the European Union's Horizon 2020 research and innovation program under grants 881603 and 764047. **Author contributions:** M.G. and D.S.K. designed and supervised the project. A.H., J.Y.K., and S.M.Z. advised on the research. M.K., J.J., and H.L. studied and constructed the concept and analyzed the experimental data. H.L., M.K., W.R.T., and J.J. wrote the manuscript. M.G. and D.S.K. revised the manuscript. T.K.L. contributed to the optical measurements. H.L., F.T.E., and W.R.T. performed the PLQY and EQE_{EL} measurements and analysis. Y.L. contributed to the characterization of the chemicals. I.W.C., S.J.C., N.G.A., S.C., and Y.J. characterized the perovskite film with UV-Vis absorption, XPS, and XRD. S.-I.M. analyzed the FTIR. H.-B.K. performed the UPS measurements. M.K., J.J., and H.L. performed the stability test. Y.-K.K. analyzed the high-resolution TEM. All authors contributed to the discussions about the manuscript and the reviewers' comments. **Competing interests:** None declared. **Data and materials availability:** All data needed to evaluate the conclusions in the paper are present in the paper or the supplementary materials.

SUPPLEMENTARY MATERIALS

science.org/doi/10.1126/science.abh1885
Materials and Methods
Supplementary Text
Figs. S1 to S29
Tables S1 to S3
References (35–50)
Movies S1 and S2

22 February 2021; accepted 7 December 2021
10.1126/science.abh1885

Conformal quantum dot–SnO layers as electron transporters for efficient perovskite solar cells

Minjin KimJaeki JeongHaizhou LuTae Kyung LeeFelix T. EickemeyerYuhang LiuIn Woo ChoiSeung Ju ChoiYimhyun JoHak-Beom KimSung-In MoYoung-Ki KimHeunjeong LeeNa Gyeong AnShinuk ChoWolfgang R. TressShaik M. ZakeeruddinAnders HagfeldtJin Young KimMichael GrätzelDong Suk Kim

Science, 375 (6578), • DOI: 10.1126/science.abh1885

Tailoring tin oxide layers

Mesoporous titanium dioxide is commonly used as the electron transport layer in perovskite solar cells, but electron transport layers based on tin(IV) oxide quantum dots could be more efficient, with a better-aligned conduction band and a higher carrier mobility. Kim *et al.* show that such quantum dots could conformally coat a textured fluorine-doped tin oxide electrode when stabilized with polyacrylic acid. Improved light trapping and reduced nonradiative recombination resulted in a certified power conversion efficiency of 25.4% and high operational stability. In larger-area minimodules, active areas as high as 64 square centimeters maintained certified power conversion efficiencies of more than 20%. —PDS

View the article online

<https://www.science.org/doi/10.1126/science.abh1885>

Permissions

<https://www.science.org/help/reprints-and-permissions>

Use of this article is subject to the [Terms of service](#)

Science (ISSN) is published by the American Association for the Advancement of Science. 1200 New York Avenue NW, Washington, DC 20005. The title *Science* is a registered trademark of AAAS.

Copyright © 2022 The Authors, some rights reserved; exclusive licensee American Association for the Advancement of Science. No claim to original U.S. Government Works